

X-ray Variability of the Seyfert 1 Markarian 335: Power Spectrum and Time Lags

P. Arévalo^{1*}, I. M. McHardy¹, D. P. Summons¹

¹*School of Physics and Astronomy, University of Southampton, Southampton SO17 1BJ, UK*

Received /Accepted

ABSTRACT

To investigate further the comparison between AGN and black hole X-ray binaries, we have studied the main X-ray variability properties of the Seyfert 1 Galaxy Mrk 335. We put particular emphasis on the X-ray time lags, which is a potentially important diagnostic of physical models. From a 100 ksec observation by *XMM-Newton* we show that the power spectrum of this source is well fitted by a bending power law model, and the bend time-scale T_b is precisely at the value predicted by the T_b vs H_β line-width relation of McHardy et al. Variations in different energy bands show time-scale dependent time lags, where higher energy bands lag lower ones. The lag, τ , varies as a function of the Fourier frequency, f , of the variability component in the light curves as $\tau \propto f^{-1}$ at low frequencies, but there is a sharp cut-off in the lags at a frequency close to the bend frequency in the power spectrum. Similar behaviour is seen in black hole X-ray binary systems. The length of the time lags increases continuously with energy separation, in an almost log-linear relation. We show that the lag spectra can be produced by fluctuations propagating through the accretion flow as long as the energy spectrum of the X-ray emitting region hardens towards the centre.

Key words: Galaxies: active

1 INTRODUCTION

Understanding the similarities between Active Galactic Nuclei (AGN), which are powered by accretion onto super-massive black holes, and the much smaller Galactic black hole X-ray binary systems (BHXRb) is currently one of the major research topics in high energy astrophysics. Although some properties might be expected to scale simply with mass, the fact that the accretion disc is much cooler in AGN may affect properties which depend on the spectrum of the nuclear ambient photon field, e.g. any X-ray emission produced by Comptonisation.

Over recent years considerable attention has been devoted to the comparison of the X-ray variability properties of AGN and BHXRb and, in particular, to comparison of their X-ray power spectrum. It has been shown that most X-ray bright AGN vary in a manner similar to that of the persistent BHXRb Cyg X-1 in the high/soft state (where the medium energy X-ray spectrum is soft and the flux is high), rather than in the low/hard state (where the medium energy X-ray spectrum is hard and the flux is low) (e.g. Uttley et al. 2002; McHardy et al. 2004, 2005; Uttley & McHardy 2005). In the soft state, the power density spectrum (PDS) of

Cyg X-1 has a power law shape of slope -1 at low frequencies (i.e. $P(f) \propto f^{-\alpha}$ with $\alpha = 1$), bending to a steeper slope ($\alpha \geq 2$) above a bend frequency f_b , and the PDS of most well observed AGN are similar. We have shown McHardy et al. (2007); K rding et al. (2007) that the time-scale associated with the bend, $T_B = 1/f_b$, scales as black hole mass divided by accretion rate (in Eddington units) from AGN down to BHXRb. As higher quality AGN X-ray data has become available, primarily from *XMM-Newton*, it is now possible to investigate other X-ray timing measurements which may, ultimately, prove to have greater diagnostic power than simple bend time-scales, i.e. X-ray time lags and coherence.

Time lags are normally observed between the fluctuations in different energy bands, where the hard X-ray bands tend to lag softer ones and the coherence is the degree to which the hard and soft bands are correlated. Where the data are good enough, the lags and coherence can be measured as a function of Fourier frequency. A particularly important aim, to which observations of lags and coherence can contribute, is to understand the origin of the X-ray variations in both BHXRb and AGN. An interesting model for the origin of the fluctuations was proposed by Lyubarskii (1997). In this model, characteristic time-scales of variability, produced by variations in accretion rate, are associated with each radius in the accretion disc, with longer time-

* E-mail: patricia@astro.soton.ac.uk

scales being associated with larger radii, and the variations propagate inward towards the X-ray emitting region. This model provides a natural explanation of the observed linear relationship between rms variability and flux in both BHXRB and AGN (Uttley & McHardy 2001).

The propagating fluctuation model has been extended by Kotov et al. (2001) and Arévalo & Uttley (2006) to include an extended X-ray emitting region where the X-ray spectrum hardens towards the black hole. As the fluctuations, which might have been produced further out, travel through this emitting region, they modulated first the emission with a softer spectrum and later the emission with harder spectra, thereby naturally giving rise to hard lags. The model has been used to simultaneously explain both the lags and the X-ray PDS in the high accretion rate Narrow Line Seyfert 1 (NLS1) Ark 564 (McHardy et al. 2007) but it has not yet been widely applied to other AGN. In this paper we analyse a long *XMM-Newton* observation of the X-ray bright NLS1 Mrk 335 and show how the propagating fluctuation model can simultaneously explain the lags and the PSD. Using our new measurement of T_B , we also investigate how well Mrk 335 agrees with the relationship between T_B and the width of the H_β emission line of (McHardy et al. 2007).

The paper is organised as follows: we briefly discuss the data reduction in section 2, calculate the power spectrum and fit it with a bending power law model in Sec. 3. We study the relation between different energy bands in Sec. 4 for the coherence and Sec. 5 for the time delays. In Sec. 6 we summarize the main variability properties of Mrk 335 found in this work.

2 THE DATA

Mrk 335 was observed by *XMM-Newton* for ~ 130 ks in 2006 January 3–5 during revolution 1112. Spectral fitting and spectral variability analyses of these data have been published by O’Neill et al. (2007) and Larsson et al. (2007).

We used data from the EPIC PN detector (Strüder et al. 2001). The PN camera was operated in Small Window mode, using thin filter. The data were processed using XMM-SAS v 6.5.0. Source photons were extracted from a circular region of $5'$ in radius and a background region of equal area was chosen on the same chip. Source and background events were selected by quality flag=0 and patterns=0–4, i.e. only single and double events were used. The background level was generally low and stable, except at the beginning and at the end of the observation. We discarded the first 10 ks and last 12.4 ks to obtain 110.6 ks long light curves free of background flares.

For the power spectrum and cross spectrum analyses, we constructed light curves in the 0.2–0.6, 0.6–1, 1–3 and 3–10 keV bands, using 54 sec long time bins, with average count rates of 9.4, 4.5, 4.2 and 0.8 counts/sec, respectively. The bin size was chosen to obtain 2^{11} points in each light curve, which enables us to use the fast Fourier transform (FFT) in the power spectrum fitting procedure.

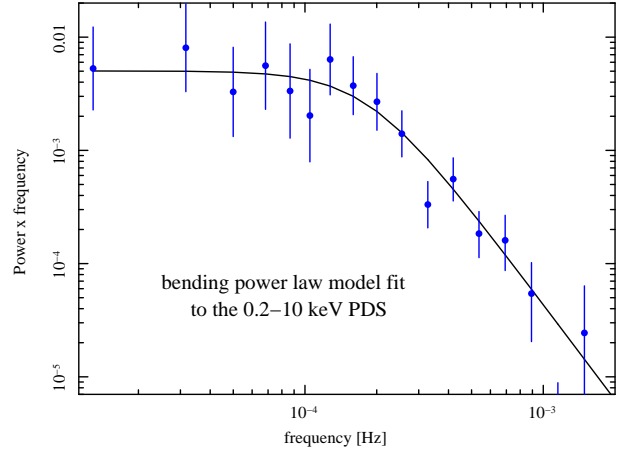


Figure 1. 0.2–10 keV PDS of Mrk 335 plotted in blue dots with error bars, with the best-fitting bending power law model plotted as a solid black line. The power due to Poisson noise, which starts to dominate the variability at 10^{-3} Hz, has been subtracted.

3 POWER SPECTRUM

All the measured AGN power spectra have an approximately $P \propto 1/f$ shape, breaking to a steeper slope at high frequencies (e.g. Uttley et al. 2002; Markowitz et al. 2003; McHardy et al. 2005, 2004; Markowitz et al. 2007), similar to the PDS of Cyg X-1 in the high/soft state. In only one AGN, Ark 564, an additional, low frequency break has been significantly detected, below which the PDS levels off to a constant value (McHardy et al. 2007). This shape resembles Cyg X-1 in either the low/hard or very high states, which have roughly a doubly-broken power law shape. In either case, single or double break, the high frequency end of the PDS has approximately a bending power-law shape with a low frequency slope of -1. For the PDS of Mrk 335 we will consider a low frequency slope of this value to test whether a high frequency bend is required by the data within the observed frequency band.

We constructed the PDS of Mrk 335 light curves through the discrete Fourier Transform (DFT) (Press et al. 1992),

$$P(f_i) = \frac{2}{\bar{x}^2} \frac{\Delta t}{N} |\text{Re}_X^2(f_i) + \text{Im}_X^2(f_i)|, \quad (1)$$

where $\text{Re}_X(f_i)$ and $\text{Im}_X(f_i)$ are the real and imaginary parts of the discrete Fourier transform of the time series $x(t)$, \bar{x} is the average count rate, Δt is the sampling time interval and N is the number of points in the light curve. With this normalisation, the power spectrum is given in terms of σ^2/\bar{x}^2 with units of $1/\text{Hz}$ so the integral of $P(f)$ over f equals the normalised variance. We binned the periodogram points in frequency bins, adopting the logarithmic binning method described by Papadakis & Lawrence (1993). A minimum of 2 points were included in each frequency bin and the bin width was set at $1.3 \times f_i$, where f_i is the smallest Fourier frequency in the corresponding bin.

We fitted a bending power law model defined as

$$P(f) = \frac{A f^{-\alpha_L}}{1 + (f/f_b)^{\alpha_H - \alpha_L}} \quad (2)$$

to the PDS of the 0.2–10 keV light curve. The low frequency slope $\alpha_L = 1$ was fixed and the high frequency slope α_H ,

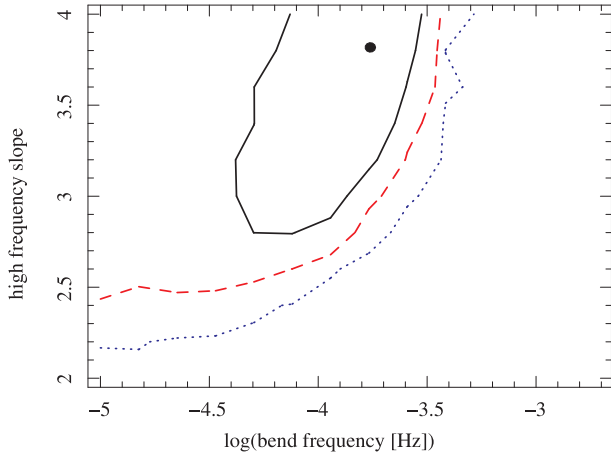


Figure 2. Confidence contours of the bending power law fit to the 0.2–10 keV PDS. The 68%, 90% and 99% levels are shown by the solid, dashed and dotted lines, respectively. The best fitting values are marked by the black dot.

the bend frequency f_b and the normalisation A were left as free parameters. We used the Monte Carlo fitting procedure PSRESP of Uttley et al. (2002), to take into account possible distorting effects of red-noise leak and aliasing and produce robust error bars and goodness of fit criteria.

The parameter space was searched over a grid of multiplicative factor 1.5 in f_b , from 10^{-5} to $10^{-2.5}$ Hz, and an additive factor 0.2 in α_H , from 1 to 4. A finer grid, with steps of 1.1 in f_b and 0.1 in α_H was used to search over the best fitting region and the resulting parameter values were essentially the same.

The best-fitting bending power law model, together with the data PDS, unfolded by observational biases, is shown in Fig. 1. This model produces a good fit with acceptance probability of 87%. The high frequency slope has a value of $\alpha_H = 3.8$ with a 90% confidence lower limit of 2.5 and a 99% limit of 2.2. This slope is therefore significantly different to the low frequency slope of 1 and the bend in the PDS is clearly detected. The best-fitting bend frequency has a value of $1.7^{+0.85}_{-1.2} \times 10^{-4}$ Hz, where the uncertainties correspond to 1σ errors. The lower 90% confidence limit on the bend frequency, however, falls below 10^{-5} Hz, which is the lowest frequency probed. Figure 2 shows the confidence contours of this fit over the entire parameter space explored. As shown below, the bend in the PDS appears to shift to higher frequencies for higher energy bands. The 99% confidence lower limit on the bend frequency falls inside the available parameter space for the 1–3 and 3–10 keV bands. Figure 3 shows the confidence contours of the fit to the 1–3 keV band PDS, where the bend frequency is well bounded.

Fitting the 0.2–10 keV band PDS, allowing the low frequency slope α_l to vary produces essentially the same values: $\alpha_H = 3.8^{+***}_{-1}$, $f_b = 1.6^{+1.6}_{-1.2} \times 10^{-4}$ Hz, and a best fitting value of $\alpha_l = 1.1$, but no useful constraints can be placed on α_l .

3.1 Bend frequency vs H_β relation

McHardy et al. (2007) have shown for a sample of AGN with

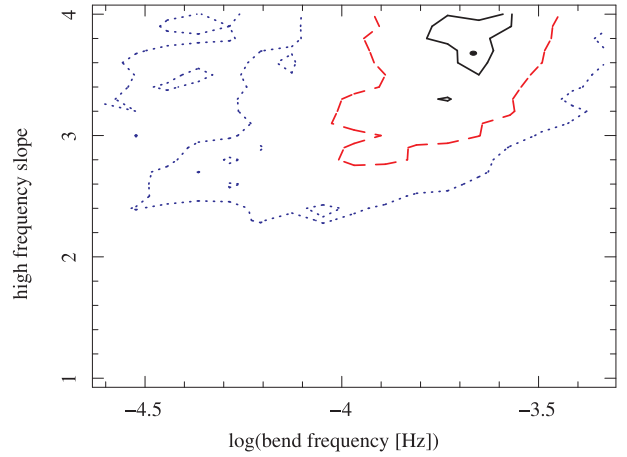


Figure 3. Confidence contours of the bending power law fit to the 1–3 keV PDS. The 68%, 90% and 99% levels are shown by the solid, dashed and dotted lines, respectively. The best fitting values are marked by the black dot. In this energy band and also in 3–10 keV, the lower 90% and 99% confidence limits on the break frequency are contained in the parameter space explored, i.e. at frequencies higher than the lowest bin frequency which is determined by the length of the observation.

Energy band [keV]	$f_b [10^{-4} \text{Hz}]$	α_h	fit probability
0.2–10	$1.7^{+0.85}_{-1.2}$	$3.8^{+***}_{-1.0}$	87.2%
0.2–0.6	$1.11^{+0.5}_{-0.71}$	$3.6^{+***}_{-1.0}$	66.9%
0.6–1	$1.55^{+1.12}_{-0.93}$	$4.0^{+***}_{-1.1}$	90.6%
1–3	$2.22^{+0.45}_{-0.36}$	$3.7^{+0.3}_{-0.4}$	41.1%
3–10	$2.38^{+1.6}_{-0.41}$	$4.0^{+***}_{-0.2}$	34.3%

Table 1. PSRESP fits to the PDS in different energy bands using a bending power law model with fixed low frequency slope $\alpha_l = 1$. The errors correspond to 66% confidence contours in the α_H vs f_b plane, asterisks denote unbounded contours.

f_b measured as above, that f_b is well correlated to the width of the H_β line in the optical spectrum, following the relation

$$\log T_b = 4.2 \log H_{\beta, \text{FWHM}} - 14.43, \quad (3)$$

where T_b is the break time-scale in units of days and $H_{\beta, \text{FWHM}}$ is in units of km/s. Peterson et al. (2004) used data from two observational campaigns to measure $H_{\beta, \text{FWHM}}$ of Mrk 335 obtaining values of 1629 ± 145 and 1375 ± 357 km/s. According to Eq. 3, these line-widths predict a break time-scale of $0.078 < T_b < 0.16$ days in the first case and $0.016 < T_b < 0.15$ days in the second. The measured bend frequency corresponds to a time-scale of $0.068^{+0.16}_{-0.023}$ days, consistent with both line width measurements, within the uncertainties. Figure 4 shows the position on Mrk 335 on the line-width vs bend time-scale plot of McHardy et al. (2007), for both line-width measurements.

3.2 Energy dependence of the PDS

The PDS of Mrk 335 shows more high frequency power at higher energies, as is normally observed in AGN (e.g. McHardy et al. 2004; Markowitz et al. 2007; McHardy et al. 2007). Fitting the 0.2–0.6, 0.6–1, 1–3 and 3–10 keV PDS with PSRESP, keeping the low slope fixed to 1, results in

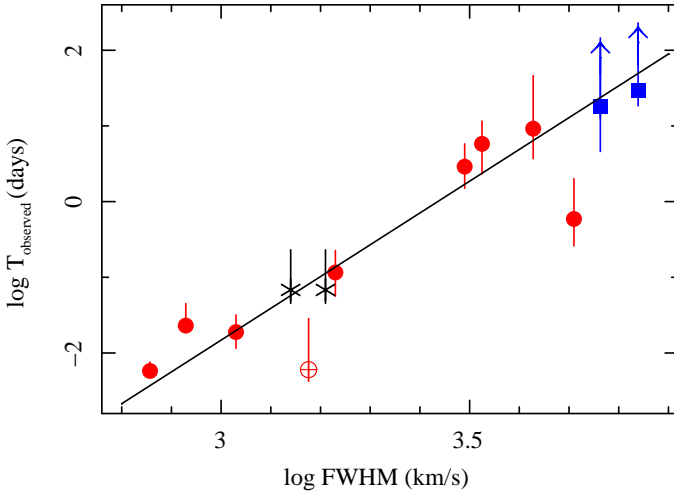


Figure 4. H_{β} line width vs break time-scale: the solid black line represents the best-fitting relation from McHardy et al. (2007) who used the 9 AGN plotted as red circles and the low luminosity AGN NGC4395 plotted as an open crossed circle. The 2 AGN (green filled squares) whose upper limit on the break time-scale is not constrained are plotted, but were not included in the fit. The black crosses represent the position of Mrk 335 on this plot, using the best-fitting break time-scale of the 0.2–10 keV PDS and the two line width measurements of Peterson et al. (2004).

higher bend frequencies for higher energy bands as shown in Table 1, although they are partly within the error from each other. The errors on these parameters are large, however, because they take into account the fact that the observation is only one realisation of a large set of possible observed PDS with the same underlying power spectrum. Considering that the observations in the different energy bands were made simultaneously, the uncertainty in the *relative* PDS shape is much smaller. To illustrate the energy dependence more clearly, we calculated the ratios of the harder band PDSs to the 0.2–0.6 keV PDS, which is shown in Fig. 5. If the energy bands were completely coherent, the only source of scatter would be the Poisson noise, which adds different amounts of power to the PDS points of each light curve, while the stochastic deviations of the coherent variations cancel out. The variations in different bands are not completely coherent, as shown below, so we considered the reduced coherence when calculating the error bars on the PDS ratio. We assumed that 10%, 20% and 40% of the fluctuations in the 0.6–1, 1–3 and 3–10 keV light curves is incoherent with the 0.2–0.6 keV fluctuations and added the uncertainty in this incoherent part of the power to the uncertainty in the power of the Poisson noise. These levels of incoherent fluctuations were chosen to match the average coherence functions between the corresponding energy bands, at least at low frequencies where the coherence can be well measured, as described in Sec. 4 below. With these error bars, the PDS ratios are not consistent with a simple change in high frequency slope to account for the additional high-frequency power, as in that case the ratios would increase as a power law instead of leveling-off and dropping. Equal power law slopes and different bend frequencies produce PDS ratios of a stepped shape, that rise rapidly at frequencies above the lower bend frequency and level-off above the higher bend fre-

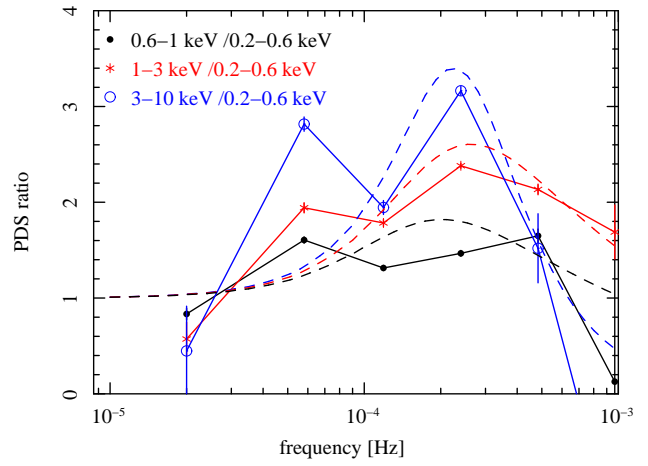


Figure 5. Additional high-frequency power at high energies: Power spectra in the 0.6–1 (black), 1–3 (red) and 3–10 keV (blue) bands divided by the PDS of the 0.2–0.6 keV band. Higher energy bands show increasingly more variability power above $\sim 2 \times 10^{-5}$ Hz.

quency. To produce a drop at even higher frequencies would require a steeper high-frequency slope for the hard band.

For visualization purposes, we over-plotted in Fig. 5 the ratios between bending power law model PDSs, with low frequency slope $\alpha_l = 1$ and different bend frequencies and α_h . For the model lines shown, we used the best fitting f_b from Table 1 for the corresponding energy bands and fixed $\alpha_h = 3$ for the soft band. We allowed α_h of the hard bands to vary in order to fit the amplitude of the PDS ratios of the data. The best fitting values of α_h were 3.5 for 0.6–1 keV, 3.6 for 1–3 keV and 4.8 for 3–10 keV. The shape of the PDS ratio indicates that higher energy bands have both a higher bend frequency and a *steeper* high frequency slope. This behaviour could indicate the presence of a band-limited high frequency variability component with a hard energy spectrum, adding on to the soft band PDS. This energy dependence, however, can also be produced by extended emitting regions filtering out the high frequency variability power. If higher energies are emitted by a more compact region, e.g. if the emitted spectrum hardens towards the centre, their PDSs will have higher bend frequencies than softer bands, while the high frequency slope can be equal or steeper (see figures 2 and 6 in Arévalo & Uttley 2006).

4 COHERENCE

We will now investigate the correlation between variations in different energy bands. The coherence γ^2 , i.e. the degree of linear correlation between two light curves, can be computed as a function of Fourier frequency using the cross spectrum $C(f) = S^*(f)H(f)$, where $S(f)$ and $H(f)$ are the Fourier transforms of the soft and hard band light curves $s(t)$ and $h(t)$, respectively.

$$\gamma^2(f_i) = \frac{\langle \text{Re}_C(f_i) \rangle^2 + \langle \text{Im}_C(f_i) \rangle^2}{\langle |S(f_i)|^2 \rangle \langle |H(f_i)|^2 \rangle} \quad (4)$$

where $\text{Re}_C(f_i)$ and $\text{Im}_C(f_i)$ are the real and imaginary parts of the cross spectrum $C(f)$ and angle brackets represent averaging over independent measurements. In our case, the in-

dependent measurements are taken from consecutive Fourier frequencies in a frequency bin. Coherence values range from 1, for totally coherent, to 0 for totally incoherent variations. See Vaughan & Nowak (1997) for a detailed description of the coherence function interpretation and error calculation.

Coherence functions were calculated between 0.2–0.6 keV and each of the three harder bands (0.6–1, 1–3 and 3–10 keV) and the results are shown in Fig. 6. A minimum of 8 points was included in each frequency bin and the bin separation was fixed at $1.5 \times f_i$.

As the Poisson noise and other distorting effects in the observed light curves can artificially decrease the coherence, we applied the Poisson noise correction factor described in Vaughan & Nowak (1997) and estimated any additional deviations using simulated light curves. For each pair of energy bands, we generated 1000 pairs of coherent red-noise light curves using the method of Timmer & König (1995), with the underlying PDS parameters obtained from the fits to the corresponding real light curves. The average count rates of the simulated light curves were made to match the measured values and Poisson deviates were added to each simulated light curve point. The coherence was then calculated for each simulated pair using the same sampling and Poisson noise correction method as used for the real data. The mean of the distribution of simulated coherence measurements for each frequency bin is plotted as a red solid line in Fig. 6 and the top and bottom 95% extremes of this distribution are plotted as dashed blue lines in the same plot.

This analysis shows that the variations in the 0.2–0.6 keV and 0.6–1 keV energy bands are highly coherent ($\gamma \sim 0.95$) up to frequencies of at least 2×10^{-4} Hz. Above this frequency Poisson noise makes the coherence estimates unreliable so it is not possible to detect a real drop in coherence. At larger separations between the energy bands the coherence drops significantly, even at the lowest frequency probed, 4×10^{-5} Hz, to ~ 0.87 between 0.2–0.6 and 1–3 keV and to ~ 0.6 between 0.2–0.6 and 3–10 keV light curves.

5 TIME LAGS

Time delays between variations in different energy bands can be measured using the phase lag spectrum $\phi(f)$. This spectrum gives the difference in phase between the Fourier transform components of the soft and hard light curves, as a function of Fourier frequency f , and it can be converted into a time-lag spectrum as $\tau(f) = \phi(f)/(2\pi f)$. See Nowak et al. (1999) for a full description of the lag spectrum measurement. In what follows we will refer to the time lag spectrum simply as lag spectrum.

In all AGN where the lag spectrum has been measured, the hard bands lag softer ones (Papadakis, Nandra & Kazanas 2001; Vaughan et al. 2003; McHardy et al. 2004; Arévalo et al. 2006; Markowitz et al. 2007) and the size of the lag increases with decreasing Fourier frequency. In the BHXRB Cyg X-1 in the high/soft state, the lag spectrum has a power law dependence on frequency with a slope of ~ 0.7 and a cut-off at high frequencies, close to the break in the PDS. In the low/hard state, the lag spectrum shows approximately the same power law dependence but with additional structure in the form of steps. AGN data are normally not good enough

to detect such structure and only simple power laws with fixed slope are fitted. A change in slope in the lag spectrum of an AGN has only been detected significantly in Ark 564 (Arévalo et al. 2006) but in that case the ‘step’ was too deep to resemble the lag spectrum of Cyg X-1 in the low/hard state and rather resembles a Very High state.

5.1 Lag spectrum

The lag spectrum of Mrk 335 between 0.2–0.6 and 3–10 keV energy bands is shown in Fig. 7, where positive values indicate hard band *lagging*. A minimum of 2 points per bin was used and the phase-lag measurements were averaged over frequency bins of width $2 \times f_i$, before being converted into time-lags. Notice that the lags are shown only for frequencies below 3×10^{-4} Hz, where the coherence is still acceptably high.

As seen in other AGN and XRB, the hard band in Mrk 335 lags the softer band and the lag size decreases with increasing frequency with an approximately power law dependence. The slope, however, appears steeper than the $\tau(f) \propto f^{-1}$ model normally fitted to AGN lag spectra.

We used simulated light curves to determine whether the steepness of the slope is produced by observational biases. Light curve pairs were generated as in Sec. 4, introducing time lags between the simulated soft and hard light curves of the form $\tau(f) = 0.082f^{-1}$, where the amplitude of the lag spectrum was obtained from a fit to the real data. The simulated light curves were sampled following the pattern of the real data and lag spectra were calculated for each pair using the same method and binning. The mean of the distribution of 1000 simulated pairs is shown by the red dotted line in Fig. 7 and the top and bottom 95% extremes of the distribution are plotted in blue dashed lines. The real lag spectrum, plotted in black markers joined by a solid line in the same figure, drops more steeply than the simulations, indicating that the drop in high-frequency lags is not due to observational biases on an intrinsically $1/f$ lag spectrum. We repeated the same experiment using the best-fitting power law model of the real data, $\tau(f) = 8.8 \times 10^{-6} f^{-1.84}$, as the underlying lag model for the simulations. In this case, the real data falls within the 95% extremes of the distribution of simulated lag spectra, but this model over predicts the scatter, putting almost the entire 95% lower limit on negative lag values. Fitting the lag spectrum with a range of slopes between -1 and -1.84 and repeating this experiment produced simulated lag distributions that are either too tight and do not include the high-frequency lag points and/or too wide and over predict the scatter in the measured lag spectrum at low frequencies. Therefore, the lag spectrum is not consistent with a single power law and the bend down or cut-off at around 10^{-4} Hz is real. Arévalo et al. (2006) found a similar change in slope in the lag spectrum of Ark 564, in that case however, the bend was found a decade in frequency below the bend frequency of the PDS, while in Mrk 335 the bend in the PDS and lag spectrum appear at the same frequency, within the uncertainties.

5.2 Energy dependence of the time-lags

The length of the time lags increases with the separation between the energies of the bands considered. We calculated

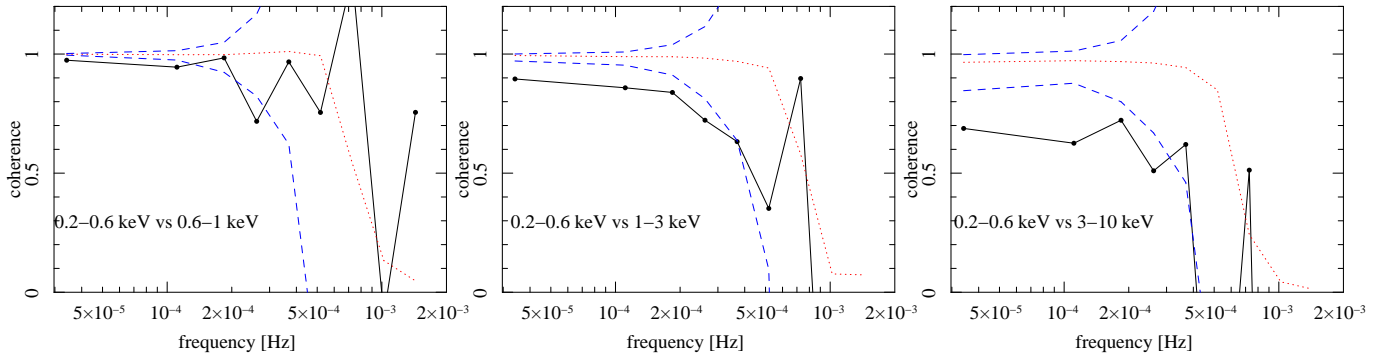


Figure 6. Coherence as a function of Fourier frequency between 0.2–0.4 and 0.4–0.6 keV energy bands (left), 0.2–0.6 and 1–3 keV bands (centre) and 0.2–0.6 and 3–10 keV bands (right), plotted in solid black lines. The dot-dashed red lines represent the median of a distribution of simulated coherence functions, constructed from intrinsically coherent light curves affected only by Poisson noise. For the simulations we used the count rate and underlying PDS shape of the corresponding light curves. The dashed blue lines represent the 95% upper and lower limits of this distribution, marking the scatter expected in the case of perfectly coherent light curves, distorted by Poisson noise and the sampling pattern in the same way as the real data. Evidently, the measured coherence is significantly lower than 1 between the 0.2–0.4 and 1–3 keV bands and between the 0.2–0.4 and 3–10 keV bands, even at the lowest frequencies sampled.

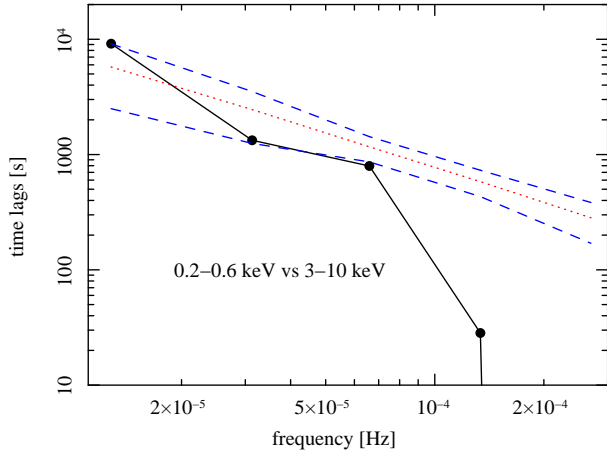


Figure 7. Time lag as a function of Fourier frequency f between the 0.2–0.4 keV and 3–10 keV energy bands over the frequency range where the coherence is well measured, the data points are shown in black markers joined by the solid line. The dotted and dashed lines represent the mean and top and bottom 95% limits of a distribution of simulated lag spectra with an underlying $lag = 0.082f^{-1}$ lag spectrum (see text). The drop of the lags at high frequencies is greater than expected for this underlying model, showing that the real lag spectrum has either a slope steeper than -1 or it cuts-off at high frequencies.

lag spectra of the 0.2–0.4 keV to the 0.4–0.6, 0.6–1, 1–2, 2–5 and 5–10 keV bands, finding that the higher the energy band, the more it lags the 0.2–0.4 keV band. The fractional lags, $\tau/\text{time-scale}$, are approximately 0.72% for 0.4–0.6 keV, 1.5% for 0.6–1 keV, 4.2% for 1–2 keV, 6.2% for 2–5 keV and 12% for 5–10 keV. Each lag spectrum resembles the one shown in Fig. 7, having a cut-off at high frequencies. These fractional lag values only represent the low-frequency part of the spectra.

In Fig. 8 we plotted the lowest-frequency lag for each pair as a function of the ratio between the average energy of the bands compared. The lags increase in an almost log-linear manner with increasing energy ratio. The best fitting

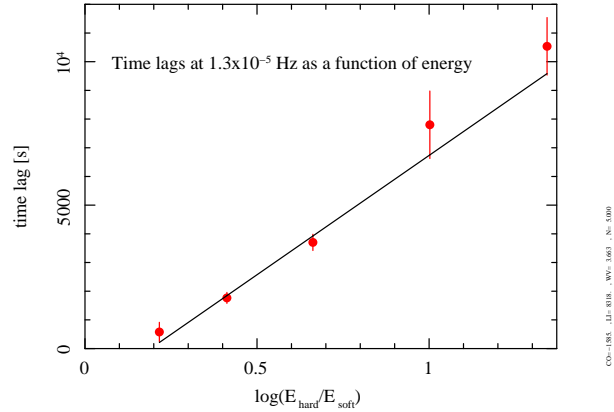


Figure 8. Time lag at frequency 1.3×10^{-5} Hz as a function of energy. The logarithm of the ratio between the average energies of the each pair of energy band is plotted in the x axis. The solid line represents a linear fit to the data plotted.

log-linear model, shown by the solid line in the plot has a form

$$\tau = (8317 \pm 1138) \log \frac{E_{\text{hard}}}{E_{\text{soft}}} - (1585 \pm 580) \text{ sec.} \quad (5)$$

For a perfect log-linear relation, the intercept should equal zero, i.e. lags between identical energy bands should be 0. The intercept of the fitted relation is significantly different from this value so the behaviour of the time lags in Mrk 335 is not entirely consistent with Cyg X-1 (Nowak et al. 1999). Notice however, that the log-linear relation in Cyg X-1 was calculated for energies above 2 keV and in Mrk 335 we used a baseline energy band of 0.2–0.4 keV. It is possible that other spectral components in Mrk 335 below 2 keV, in particular the soft excess might be suppressing the intermediate-energy lags.

5.3 Interpretation of the lag spectrum

We applied the propagating fluctuation paradigm of Lyubarskii (1997) to attempt to reproduce the observed lag

spectra. In this scenario, the fluctuations are produced by the accretion flow over a large range in radius, and travel towards the centre to modulate the X-ray emitting region. We assume that the fluctuations are produced and propagated on the viscous time-scale of a thick accretion flow and that the emitted energy spectrum hardens towards the centre, therefore producing hard lags.

The travel time tt of a fluctuation of frequency f , from its radius of origin r_f to any radius r is given by

$$tt(r) = \int_r^{r_f} \frac{dr}{v(r)} = \frac{2}{3(H/R)^2\alpha} (r_f^{3/2} - r^{3/2}) \quad (6)$$

where the second equality assumes a propagation speed $v(r) = (H/R)^2\alpha r^{-1/2}$ in units of c and r in units of $R_g = GM/c^2$. This speed is taken from the standard disc prescription (Shakura & Sunyaev 1973), where α is the viscosity parameter and H/R the disc thickness to radius ratio.

The time lags arise from different radial emissivity profiles $\epsilon(r)$ characterising the different energy bands. The weighted travel time, $\bar{\tau}(f)$ of a fluctuation on frequency f folded through a given emissivity profile is

$$\bar{\tau}(f) = \frac{\int_{r_{in}}^{r_f} tt(r)\epsilon(r)2\pi r dr}{\int_{r_{in}}^{r_f} \epsilon(r)2\pi r dr} \quad (7)$$

We will replace the normalisation factor $\int_{r_{in}}^{r_f} \epsilon(r)r dr$ by E in what follows and cancel the 2π factors. Finally, the time lag between two energy bands with emissivity profiles $\epsilon_a(r)$ and $\epsilon_b(r)$ is the difference between the corresponding weighted travel times,

$$\tau(f) = \bar{\tau}_a(f) - \bar{\tau}_b(f) = \int_{r_{in}}^{r_f} \left[tt(r) \frac{\epsilon_a(r)}{E_a} - tt(r) \frac{\epsilon_b(r)}{E_b} \right] r dr \quad (8)$$

replacing $tt(r)$ by the expression in Eq. 6 and cancelling terms gives:

$$\tau(f) = \frac{-2}{3(H/R)^2\alpha} \int_{r_{in}}^{r_f} r^{5/2} \left(\frac{\epsilon_a(r)}{E_a} - \frac{\epsilon_b(r)}{E_b} \right) dr \quad (9)$$

Notice that the length of the time lag is not simply proportional to $1/(H/R)^2\alpha$ because the integration limit r_f is also a function of these disc parameters. If the disc thickness or α decrease, the propagation speed decreases making the lag longer, but the fluctuations on a given frequency are produced at a smaller radius r_f , so they travel a shorter distance and so $\tau(f)$ remains at approximately the same level.

Equation 9 gives the lag spectrum between energy bands characterised by emissivity profiles ϵ_a and ϵ_b . From standard disc theory, the total energy dissipated per unit area follows a $\epsilon \propto r^{-3}$ relation. As a simple example we used similar power law emissivity profiles but with higher exponents for higher energy bands, to produce a spectrum that hardens towards the centre.

Kelly & Bechtold (2007) measured a mass for Mrk 335 of $6.6_{-3.2}^{+6.3} \times 10^6 M_\odot$, we used this mass estimate to calculate $R_g/c = 33 \text{ sec}$ to compare model predictions to the real data. In this model, both the bend in the PDS and the cut-off in the lag spectrum are related to the characteristic time-scale of the innermost region of the accretion flow. This normally requires thick disc parameters to produce the power observed at the highest frequencies. We used $(H/R)\alpha = 0.1$ to put the viscous time-scale, $t_v = r/v_{\text{visc}}(r)$, at a radius of $6R_g$ (i.e. the last stable orbit of a non-rotating black hole)

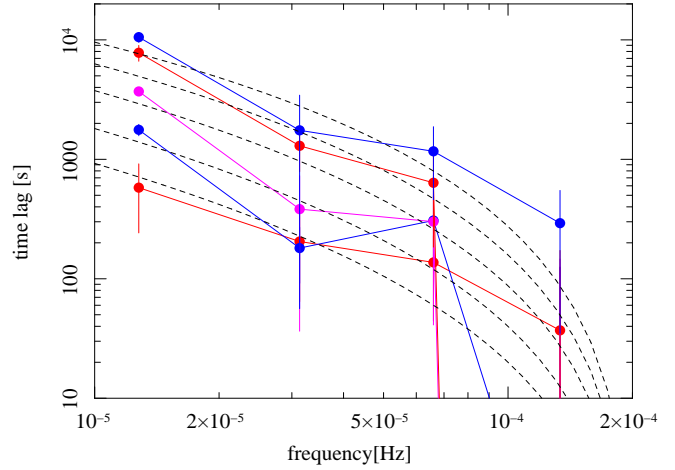


Figure 9. Time lag as a function of Fourier frequency between the 0.2-0.4 keV energy band and consecutively higher energy bands. The length of the lag increases with the separation of the energy bands. The dashed lines represent model fits as explained in Sec. 5.3

at 10^4 s for a $6.6 \times 10^6 M_\odot$ black hole, which is appropriate for modelling Mrk 335.

The measured lag spectra between the 0.2–0.4 keV band and all harder bands are shown by the markers and solid lines in Fig. 9, where the higher energy hard bands produce longer lags. The quality of the data does not allow a detailed fit to each lag spectrum but we attempted a simple implementation of the model described above to make a broad comparison. The dashed lines in Fig. 9 represent the model fits, where we assumed parameters $(H/R)\alpha = 0.1$, innermost radius of the disc $r_{in} = 6R_g$ and an emissivity profile for the 0.2–0.4 keV band of $\epsilon \propto r^\beta$ with $\beta_{0.2-0.4} = -3.0$. The other energy bands were also assumed to have power law emissivity profiles and the exponents were allowed to vary in order to fit the data. The standard viscous propagation speed resulted too high and produced lags consistently shorter than the observed values. We reduced the propagation speed by a factor of two for the fits, which reproduced the observed average lags. The models shown in Fig. 9 have exponents of -3.08, -3.15, -3.33, -3.6 and -3.8 for the 0.4–0.6, 0.6–1, 1–2, 2–5 and 5–10 keV bands, respectively.

The model does reproduce the power law shape of each lag spectrum and predicts a cut-off at the right frequency. The range of lag spectra amplitudes can be reproduced with moderate differences in the emissivity profiles of the energy bands. These energy-dependent emissivity profiles can be translated into a radial dependence of the emitted spectrum. The exponents stated above produce spectral slope changes from $\Delta\Gamma = \Gamma(r_2) - \Gamma(r_1) = 0.35 \log(r_2/r_1)$ when we compare 0.2–0.4 to 0.4–0.6 keV energy bands up to $\Delta\Gamma = 0.6 \log(r_2/r_1)$ when comparing 0.2–0.4 to 5–10 keV energy bands, where $r_2 > r_1$, $\text{flux}(E) \propto E^{-\Gamma}$ and E is the average energy of the band. This difference in spectral hardening implies that, for the model to work exactly, either the radial emissivity profiles are not exact power laws or that the emitted spectrum at each radius is not a power law.

As Mrk 335 is accreting at a high rate, an accretion disc with constant scale height H , at least at the centre, can be more appropriate. Svensson & Zdziarski (1994) solve the

structure equations of a thin disc plus corona system, and show that the accretion flow represented by the corona is radiation pressure dominated at accretion rates above approximately 18% the Eddington limit. As this is probably the case in Mrk 335, if we identify the corona with the accretion flow producing and propagating the variability, we should consider a scale-height radial dependence of $H/R = r^{-1}\dot{m}(1 - \sqrt{6/r})/2$. Assuming that the same viscous velocity prescription applies in this case, then the propagation velocity will contain an additional factor of r^{-2} which reflects the change in $(H/R)^2$ with radius, i.e. $v = (H/R)_o^2 \alpha r^{-5/2}$, where $(H/R)_o^2$ is a fixed value. The resulting travel time of the fluctuations changes to $tt(r) = \frac{2}{7(H/R)_o^2 \alpha} (r_f^{7/2} - r^{7/2})$, which can then be used in Eq. 8 to calculate the lag spectra. The shape of the lag spectra are approximately the same as in the case of constant $(H/R)^2$, shown in Figure 9. As long as the factor $(H/R)^2 \alpha$ is the same at the innermost radius, the constant H/R and constant H models produce the bend at the same frequency. The constant H model however produces even shorter lags, by approximately a factor of 4, so for this model to produce the observed lag values the propagation speed should be reduced by a factor of ~ 8 compared to the viscous velocity.

6 DISCUSSION AND CONCLUSIONS

We have studied the standard variability properties of Mrk 335 using a 114 ks observation by *XMM-Newton*. The main results are summarized below.

- The Power spectrum is well described by a bending power law model, with low frequency slope fixed at $\alpha_l = 1$, best-fitting bend frequency of $f_b = 1.7_{-1.2}^{+0.85} \times 10^{-4}$ Hz and high frequency slope of $\alpha_h = 3.8_{-1.0}^{+**}$.
- The measured bend frequency coincides precisely with the value predicted by the f_b vs H_β line-width relation of McHardy et al. (2007), using the H_β line-width measurements of Peterson et al. (2004), which demonstrates the validity of this relation.
- The power spectrum is energy-dependent with more high-frequency power at higher energies. The difference in the PDSs of different energy bands indicates a shift in the PDS bend to higher frequencies for higher energy bands.
- The degree of coherence between variations in different energy bands decreases with the energy separation of the bands considered. The coherence is significantly lower than 1, between the 0.2–0.6 and the 1–3 keV and 0.2–0.6 and 3–10 keV energy bands, even at the lowest frequencies sampled (4×10^{-5} Hz).
- Time lags are found between variations in different energy bands, where harder X-rays lag softer bands. The lag spectrum as a function of Fourier frequency can be fit with a single power law of slope ~ -1.8 , much steeper than the lag spectra observed in other AGN. Alternatively, the lag spectrum of Mrk 335 is consistent with a power law of slope ~ -1 dropping to a steeper slope at around 10^{-4} Hz, where the bend in the PDS is also found. The latter shape resembles the high frequency end of lag spectra of Cyg X-1 in both low/hard and high/soft states.
- The size of the time lags increases with energy separation following an almost log-linear relation. In all cases

tested, using the energy bands 0.2–0.4, 0.4–1, 1–2, 2–5 and 5–10 keV, any band lags all softer ones, at least at low frequencies where the error bars are small.

Arévalo & Uttley (2006) have shown that the propagating-fluctuation paradigm of Lyubarskii (1997) reproduces the shape of the PDS and the rms-flux relation. This variability model is successful in producing variability over a very broad range of time-scales and it naturally predicts a cut-off at high frequencies. Complemented with an extended emitting region whose spectrum hardens towards the centre, this model can explain the time lags (Kotov et al. 2001) and is compatible (but does not ensure) high coherence in the fluctuations of different energy bands. The extent of the emitting region in the model also acts as a low-pass filter reducing the high frequency power in the more extended energy bands, i.e. the softer bands, shifting the bend frequency to lower values.

The energy dependence of the PDS, together with the shape of the lag spectra of Mrk 335 are consistent with the predictions of this model, if the propagation speed is reduced by a factor of 2–8, compared to the viscous velocity, depending on the disc structure. The lag spectra can be reproduced by a simple implementation of the model, with an emitted energy spectrum that hardens towards the centre. The energy dependence of the length of the time lags requires a maximum hardening of the spectrum with decreasing radius, between any radii r_1 and r_2 , of $\Delta\Gamma = 0.6 \log(r_2/r_1)$.

ACKNOWLEDGEMENTS

We thank the referee for providing useful comments. This work has made use of observations obtained with *XMM-Newton*, an ESA science mission with instruments and contributions directly funded by ESA member states and the US (NASA). PA and IMcH acknowledge support from STFC under rolling grant PP/D001013/1

REFERENCES

- Arévalo P., Uttley P., 2006, MNRAS, 367, 801
 Arévalo P., Papadakis I.E., Uttley P., McHardy I.M., Brinkmann W., 2006, MNRAS, 372, 401
 Kelly B., Bechtold J., 2007, ApJS, 168, 1
 Körding E. G., Migliari S., Fender R., Belloni T., Knigge C., McHardy, I., 2007, MNRAS, 380, 301
 Kotov O., Churazov E., Gilfanov M., 2001, MNRAS, 327, 799
 Larsson J., Miniutti G., Fabian A. C., Miller J. M., Reynolds C. S., Ponti G., 2007, arXiv0712.1906
 Lyubarskii Y. E., 1997, MNRAS, 292, 679
 Markowitz A., Papadakis I., Arévalo, P., et al., 2007, ApJ, 656, 116
 Markowitz A., Edelson R., Vaughan S., et al. 2003, ApJ, 593, 96
 McHardy I. M., Arévalo, P., Uttley P., et al., 2007, MNRAS, 382, 985
 McHardy I. M., et al., 2006, Nature, 444, 730
 McHardy I. M., Papadakis I. E., Uttley P., Page M. J., Mason K. O., 2004, MNRAS, 348, 783

- McHardy I. M., Gunn K.F., Uttley P., Goad M.R., 2005, MNRAS, 359, 1469
- Nowak M., Vaughan B., Wilms J., Dove J., Begelman M., 1999, ApJ, 510, 874
- O'Neill P. M., Nandra K., Cappi M., Longinotti A. L., Sim S. A., 2007, MNRAS, 381, L94
- Papadakis I. E., Nandra K., Kazanas D., 2001, ApJ, 554,133
- Papadakis I. E., Lawrence A., 1993, MNRAS, 261, 612
- Peterson, B. M.; Ferrarese, L.; Gilbert, K. M. et al., 2004, ApJ, 613, 682
- Press W.H., Teukolsky S.A., Vetterling W.T., Flannery B.P., 1992, Numerical Recipes. Cambridge University Press, Cambridge
- Shakura N.I., Sunyaev R., 1973, A&A, 24, 337
- Strüder, L., Briel, U., Dennerl, K., et al. 2001 A&A, 365, L18
- Svensson R., Zdziarski A., 1994, ApJ, 436, 599
- Uttley P., McHardy I. M., Papadakis I. E., 2002, MNRAS, 332, 231
- Uttley P., McHardy I. M., 2005, MNRAS, 363, 586
- Uttley P., McHardy I. M., 2001, MNRAS, 323, 26
- Vaughan B., Nowak M., 1997, ApJ, 474, L43
- Vaughan S., Fabian A.C., Nandra K., 2003, MNRAS, 339, 1237
- Timmer J., König M., 1995, A&A, 300, 707